Microstructure, tensile and fatigue properties of ultrasonic spot welded aluminum to galvanized high-strength-low-alloy and low-carbon steel sheets

F.A. Mirza [a], A. Macwan [b], S.D. Bhole [b], D.L. Chen [b,*] and X.-G. Chen [a,*]

[a] *Department of Applied Sciences, University of Québec at Chicoutimi*

555, boulevard de l'Université, Chicoutimi, QC G7H 2B1, Canada

[b] *Department of Mechanical and Industrial Engineering, Ryerson University,*

350 Victoria Street, Toronto, Ontario M5B 2K3, Canada

Abstract

The microstructure evolution, tensile lap shear strength and fatigue properties of dissimilar ultrasonic spot welded (USWed) joints of aluminum to two commercial steel sheets at different welding energies were investigated. The main intermetallics at the weld interface were θ ($FeAl_3$) in both joints along with eutectic Al-Zn in Al-to-galvanized high-strength-low-alloy (HSLA) steel joints and Fe_3Al in Al-to-ASTM A36 steel joints. The welding strengths of both joints were higher than those of other dissimilar joints reported in the literature. With increasing welding energy, the maximum tensile lap shear strength increased in the Al-to-galvanized HSLA steel joints, while the lap shear strength increased up to a peak value and then decreased in the Al-to-ASTM A36 steel joints. Both the average peak welding strength and fracture energy of the Al-to-galvanized HSLA steel joints were higher than those of the Al-to-ASTM A36 steel joints. The fatigue lives of both welded joints were in agreement with or somewhat longer than other Al-to-

*Corresponding authors – X.-G. Chen, Tel: (418) 545-5011 ext. 2603; Fax: (418) 545-5012; Email: xgrant.chen@uqac.ca and D.L. Chen, Tel: (416) 979-5000 ext. 6487; Fax: (416) 979-5265; Email: dchen@ryerson.ca.

steel USWed joints in the literature. The fatigue fracture mode changed with increasing cyclic loads in both welded joints. Fatigue crack growth was mainly characterized by the formation of fatigue striations perpendicular to the fatigue crack propagation direction.

Keywords: Dissimilar ultrasonic spot welding; Tensile lap shear strength; Fatigue life and fracture; Aluminum alloy; Steel alloy; Interface microstructure.

1. Introduction

In recent years, lightweighting in vehicles has become a crucial approach for improving fuel efficiency and reducing climate-changing CO_2 emissions [1,2]. The desire to find alternative solutions has driven the automotive and aerospace industries towards improving vehicle performance and fuel economy [2]. Hence, lightweight aluminum (Al) alloys have become increasingly popular in the fabrication of vehicles due to their high strength-to-weight ratio, good formability, machinability, environmental friendliness and recyclability [3-6]. Developing lower-cost joining techniques is key to expanding the use of Al alloys in auto body manufacturing [4], and the use of hybrid structures made by dissimilar joining techniques has now become necessary [7]. In recent years, multimaterial fabrication, especially the joining of galvanized high-strength-low-alloy (HSLA) steel sheets with competitive structural grades of Al alloys to reduce the overall vehicular weight has gained significant attention in the automotive industry [3,7]. Unlike high energy consuming resistance spot welding (RSW) (20 kWh) [4] and friction stir spot welding (FSSW) (2 kWh) [8], the welding of Al alloys using a USW process consumes less welding energy (~0.3 kWh per 1000 joints) [4,9,10]. Additionally, the peak temperature during USW does not surpass the melting point of the metal workpiece, eliminating the formation of undesirable compounds and metallurgical defects that are commonly observed in most other fusion welds [11]. USW is already considered to be an emerging and promising technique for joining non-ferrous metals and alloys (maximum sheet thickness of 1-2 mm) as well as welding dissimilar material combinations [4,12].

Previous studies have shown that one of the most detrimental issues during rapid solid-state welding process such as USW is control of the intermetallic compounds (IMCs) that form at the weld interface via an accelerated diffusion process [3,10,13]. These IMCs are brittle, and a

continuous IMC interface layer severely deteriorates the joint strength [3]. For example, Haddadi [14,15] reported that the lap shear peak load decreased from 3.1 kN to 1.7 kN with increasing welding time due to an increase in brittle Fe_2Al_5 and $FeAl_3$ IMCs at the interface of Al to steel USWed joints. In addition, many studies have used interlayers or coatings to either inhibit their growth or avoid the formation of IMCs or form relatively ductile IMCs [12,13]. Watanabe *et al.* [13] used commercially pure Al sheet as an insert metal in the USW of Al-to-mild steel to study the effects of insert metals on joint properties. Patel *et al.* [3] and Haddadi *et al.* [12] have used zinc coated steel to inhibit/eliminate Al-Fe IMCs during Al-steel USW joining and showed improved mechanical properties. The composition of the weld materials can strongly affect IMC formation at the joint interface in dissimilar welding [16], although the relationship to many common alloy additions is still unknown. To the best of our knowledge, there are no systematic studies on the effect of interlayers on the formation of IMCs and the subsequent monotonic and cyclic properties of USWed dissimilar joints in the open literature. Many studies have reported squeezing of eutectic Al-Zn during USW of Al to Zn-coated steel [3,12]; however, its role in the mechanical properties of the joints has not yet been clearly understood. In addition, there is no information addressing any kind of comparison between USWed galvanized high strength low alloy steel and low carbon steel joints. The present study was, therefore, aimed at gaining a better understanding of the influence of interlayers on the formation of IMCs along with investigating the interface microstructures, tensile lap shear strengths and fatigue properties of two USWed dissimilar Al-to-steel joints.

2. Materials and Experimental Procedure

The USWed joints were produced using commercially available 1.5 mm thick sheets of Al 6061-T6 alloy and two commercial steels (a cold-rolled hot-dip galvanized HSLA steel and a low-carbon ASTM A36 steel). The nominal chemical composition of test materials used is given in Table 1. The sheet surfaces were ground using 120 grit sand paper, cleaned with ethanol followed by acetone, and dried before welding. The lap tensile test samples were welded in an energy mode using 15 mm × 60 mm strips using a Sonobond dual-head spot welding system, with the weld located at the center of a 20 mm overlap. A transverse relative displacement between the sheets with the vibration direction perpendicular to the rolling direction was applied during USW. Welding was carried out at different welding energies ranging from 500 to 1750 J by varying the welding time (t) from 0.25 to 0.875 s at a constant power of 2 kW, an impedance setting of 8 and clamping pressure of 0.4 MPa. The welding energy is determined by the relation $Q \sim P \times t$, where Q is the weld energy and P is power, e.g., the weld time of 0.75 s at 2 kW power corresponds to ~ 1500 J of welding energy.

The metallographic samples were prepared from welded joints (sectioned across the center parallel to the direction of vibration in the wedge-reed system) using a slow-speed diamond cutter and then the sample preparation was done using standard metallographic techniques. Microstructure examinations were performed using a scanning electron microscopy (SEM, JEOL JSM-6480LV) equipped with energy dispersive X-ray spectroscopy (EDS). A computerized Buehler hardness testing machine was used for the microhardness tests on the polished surface in the vicinity of the interface using a dwell time of 15 s. Special attention was paid during the hardness tests to keeping adequate space to avoid any potential effect of the strain field caused by adjacent indentations. To estimate the joint strength, tensile lap shear tests were performed for

each welding condition using a fully computerized United Mechanical Testing Machine at room temperature at a constant crosshead speed of 1 mm min^{-1}. As indicated above, both the lap shear tensile test and fatigue test specimens were 60 mm length and 15 mm width at 20 mm over lapped position. The total failure energy was calculated from the area under the load-displacement curve up to the peak failure load. Phase identification on both matching surfaces of the Al and steel was performed after the tensile shear tests using a PANalytical X-ray diffractometer (XRD) with Cu K_α radiation at 45 kV and 40 mA in back reflection mode. The diffraction angle (2θ) at which the X-rays hit the samples varied from 20 to 100°, with a step size of 0.05° and 2 s at each step. Load-control fatigue tests were performed in accordance with ASTM E466 on a fully computerized Instron 8801 servo-hydraulic testing system at different maximum loads. To avoid potential buckling of the test specimens, tension-tension cyclic loading at a stress ratio of R (P_{min}/P_{max}) = 0.2 was applied at a frequency of 50 Hz with a sinusoidal waveform. At least two samples were tested at each energy level for both the tensile lap shear tests and the fatigue tests. To minimize the phase angle and the resulting bending moments of the specimens during the tensile lap shear and fatigue tests, two spacers or restraining shims were attached at both ends of the specimen. The tensile and fatigue fracture surfaces were examined via SEM.

3. Results and Discussion

3.1 Microstructure evolution

For solid-state welded joints of dissimilar metals, there are two main factors controlling the joining performance [6]. One is the intimate contact between the dissimilar materials, and the other is the microstructure, particularly the formation of IMCs. In the present study,

microstructural characterization was conducted on the cross-section of selected welded samples at various welding energy values (500 to 1750 J) to investigate the relationship between physical weld attributes and weld performance. Fig. 1 shows the microstructures of dissimilar USWed Al 6061-to-galvanized HSLA steel and Al 6061-to-ASTM A36 steel joints at different welding energy levels. As seen from Fig. 1, there were no large defects, such as cracks, voids or tunnels, present in the samples under most of the welding conditions, indicating overall good bonding under all of the welding conditions. It is apparent from the SEM images (Figs. 1(e) and (f)) that almost sound joints were achieved by increasing the welding energy up to 1500 J. Furthermore, it is seen from Figs. 1(c), 1(d), and 1(f) that interface bonding also occurred via mechanical interlocking due to solid-state deformation at higher welding energy levels of 1000 J to 1500 J as well as the formation and progressive spreading of microwelds. This is related to the considerable increase in temperature in the weld zone, which softens the material and allows the sonotrode tips to sink into the sheet surfaces. In the process, the weld interface is displaced into complex wave-like flow patterns as indicated by the yellow dashed circles (Figs. 1(c), 1(d), and 1(f)). A similar phenomenon was also reported in Refs. [9,10,12,17]. It is also obvious from the SEM images of dissimilar USWed Al 6061-to-galvanized HSLA steel welds (Figs. 1(a), (1c), and 1(e)) that an Al-Zn-enriched non-uniform layer was observed at the interface between the Al and Fe substrate under most of the welding conditions. The thickness of the Al-Zn layer increased with increasing energy input. At higher energy inputs (1000 J and 1500 J), the welded specimen was subjected to higher temperatures under a larger vibration amplitude for a longer time, resulting in more of the Zn interlayer being squeezed out, as indicated by the arrows in Figs. 1(c) and 1(e).

To identify the possible phases during the USW, EDS line scan analysis was performed across the center of the nugget zone of Al 6061-to-galvanized HSLA steel and Al-to-ASTM A36 steel joints at a welding energy of 1000 J (Fig. 2). A relatively larger interface diffusion layer was formed in Al 6061-to-galvanized HSLA steel joints compared with Al-to-ASTM A36 steel joints. As reported by Patel *et al.* [3] and Xu *et al.* [18], this layer could be the IMCs containing Al and Fe and these IMCs formed along the bonding line of welds through interdiffusion. At a distance of approximately 4 μm (Fig. 2(c)), the concentration of Al started to decrease. However, as shown in (Fig. 2(a)) and 2(c)), there was higher concentrations of Al and Zn than Fe in the center of the nugget zone (Region 1). According to the Al-Zn binary phase diagram [19] and EDS line analysis results, Region 1 could be the eutectic film of Al-Zn. It was reported that the weld temperature at the center of the joint line was expected to exceed the Al-Zn eutectic melting point of 655 K (382°C) [3]. Due to the longer weld times, the excess Al-Zn eutectic liquid would be squeezed out from the nugget area to form a thin eutectic film (Figs. 1(a), (c), and (e)). Patel *et al.* [3], Haddadi *et al.* [12] and Ueda *et al.* [20] also reported the formation of this type of Al-Zn eutectic liquid in USW and RSW of Al-to-galvanized steel joints. There is another region (Region 2) between the Al-Zn eutectic film and Fe matrix, as indicated in the EDS line scan (Fig. 2(c)). The situation in the USWed Al 6061-to-ASTM A36 steel joints was quite straight forward (Figs. 2(b) and (d)). At a distance of ~4.5 μm (Fig. 2(d)), the concentration of Al started to decrease, then suddenly spiked at a distance of ~5 μm and finally decreased again. The line scan results clearly shows that more Fe merged with Al at a distance of ~6 μm, which then increased. According to the Al-Fe binary phase diagram, Al has a fairly high solubility in Fe and it can form disordered solid solution in Fe up to ~11 wt.% of alloying [21]. Beyond this critical amount of Al, some brittle IMCs such as θ ($FeAl_3$), η (Fe_2Al_5), $FeAl_2$, and FeAl would emerge

[3,9,12,18]. Many studies have also reported the presence of these IMCs during the welding of Al and steel, which is the main cause of fractures [3,18].

Fig. 3 shows the X-ray diffraction patterns obtained on both matching fracture surfaces of the Al and steel for both the USWed Al-to-galvanized HSLA steel joints and the Al-to-ASTM A36 steel joints after the tensile lap shear test. It is clear that, in addition to strong Al peaks (Fig. 3(a)) for Al-to-galvanized HSLA steel joints, peaks of θ ($FeAl_3$) appeared on both sides of the fracture surfaces and Zn peaks appeared on the steel side. As mentioned earlier, many studies have reported the presence of the θ ($FeAl_3$) brittle phase during the welding of Al-to-steel [13,22-25] even in USWed joints [3,4,9,18,14]. Haddadi *et al.* [12] have reported the formation of brittle IMCs of Fe_5Zn_{21} and Fe_3Zn_{10} in USWed Al-to-galvanized steel joints. However, in the present study, no peak was found for the Fe-Zn IMCs. On the other hand, for Al-to-ASTM A36 steel joints, peaks of two IMCs, θ ($FeAl_3$) and Fe_3Al, were found on both sides of the fracture surfaces. The first phase of θ ($FeAl_3$) that forms during metal-to-metal interaction is the phase with negative free Gibbs energy that is kinetically favored [14]. In the later stage, the θ ($FeAl_3$) and Fe phases react with each other to form phases such as η (Fe_2Al_5), $FeAl_2$, FeAl, and Fe_3Al [16,25-27]. This is in agreement with the results presented here (Fig. 3(b)), showing both θ ($FeAl_3$) and Fe_3Al IMCs in USWed Al-to-ASTM A36 steel joints. The presence of Fe_3Al was also confirmed in Al-to-ASTM A36 steel joint as reported in laser beam lap joints of A6111-to-cold-rolled steel plates (SPCC) by Lee *et al.* [28]. The main difference between Al-to-galvanized HSLA steel and Al-to-ASTM A36 steel joints is peaks of Zn in addition to the common θ ($FeAl_3$) phase in both joints.

3.2 Microhardness

Microhardness profiles across the interfaces of dissimilar USWed Al-to-galvanized HSLA steel and Al-to-ASTM A36 steel joints at different levels of welding energy are shown in Fig. 4. It is clear from both hardness profiles that no noticeable heat-affected zone (HAZ) was present. Similar results have been reported for USW joints [3,29]. Obvious asymmetrical hardness profiles across the interfaces of both dissimilar joints were obtained with an average hardness value of 47-57 HV on the Al side, ~153 HV on the galvanized HSLA steel side and ~129 HV on the ASTM A36 steel side. Compared to the ASTM A36 steel, a higher hardness in the galvanized HSLA steel side was observed, which is due to the high strength of the bulk galvanized HSLA steel. In general, the hardness is supposed to decrease with increasing welding energy due to increasing grain size with increasing temperature [30,31]. As seen in Fig. 4, in contrast to the present work, the hardness values on the Al and Fe sides of both the galvanized HSLA steel joints and the ASTM A36 steel joints were constant within the experiment scatter with increasing temperature.

3.3 Lap shear tensile strength and failure mode

The maximum tensile lap shear strengths of dissimilar USWed Al-to-galvanized HSLA steel joints and Al-to-ASTM A36 steel joints were plotted against the welding energy at a constant power of 2000W and constant clamping pressure of 0.4 MPa as shown in Fig. 5. The tensile lap shear strength of Al-to-ASTM A36 steel joints increased with increasing welding energy up to 1500 J, where it reached its average maximum value of ~69 MPa (calculated as the maximum tensile lap shear load divided by the sonotrode area of 8 × 5 mm^2) and decreased with further increases in the welding energy. This is due to the growth of the brittle IMC phases (θ ($FeAl_3$) and Fe_3Al). These IMC phases have inherently low ductilities that compromise the integrity of

the joint [3]. The trend was different in the case of Al-to-galvanized HSLA steel, where the lap shear strength increased with increasing welding energy and reached its highest value of ~84 MPa at 1750 J. In addition, Patel *et al.* [3] reported that the strength decreased with further increases in the welding energy, i.e., 2500 J and 3000 J. Fig. 6 shows a comparison of the maximum lap shear strength of dissimilar Al-to-steel joints with different alloys and produced by different joining techniques [4,14,15,20,32-35]. The approximate strength was calculated by dividing the maximum failure load with area, where the area was calculated using the sonotrode tip size for USW, electrode diameter for RSW, and shoulder and pin diameter for FSSW, respectively. It can be seen from Fig. 6 that the welding strengths of both joints were higher than that of other dissimilar joints reported in the literature. The strength of USWed Al-to-galvanized HSLA steel joints (~84 MPa (~3.4 kN)) showed the highest value compared to various alloys combinations and various welding techniques [4,14,15,20,32-35]. On the other hand, the USWed Al-to-ASTM A36 steel joints (~69 MPa (~2.7 kN)) exhibited higher strengths than the other USWed Al-to-steel joints [4,14,15], and these joints showed even better joining strengths when compared to different welding techniques, i.e., RSWed Al 6111-to-colled rolled steel [20] and FSSWed AA6063-to-low carbon galvanized high strength steel [33,34]. In comparison with the lap shear strengths, the fracture energies of the welded joints exhibited a larger scatter (Fig. 7). The optimum welding energy resulted in a peak value of the fracture energy followed by a decrease. In addition, the USW process for the dissimilar joints can also be compared with other spot welding processes. For instance, Fukumoto *et al.* [36] obtained a 3.5 kN lap shear peak load with a longer welding time of 5 s using friction stir spot welding compared with the current study (e.g., 3.3 kN and 3.4 kN with much shorter welding times of 0.75 s and 0.875 s, respectively). Thus, the current results point to promising solutions for dissimilar metal joining.

Fig. 8 shows the effect of the welding energy on the average tensile lap shear peak loads of dissimilar USWed Al-to-galvanized HSLA steel and Al-to-ASTM A36 steel joints along with typical tensile failure locations and modes as shown in Fig. 9. The lap shear tensile fracture occurred from the Al/Fe interface in the case of lower energy inputs (e.g., 500 J and 1000 J for both Al-to-galvanized HSLA steel (Figs. 9(a) and (b)) and Al-to-ASTM A36 steel joints (Figs. 9(e) and (f)). This is because, at lower energy inputs, the weld interface temperature was not high enough to soften the sample or diffuse the Zn interlayer into the Al to achieve a sound joint [3], which was also verified by microstructure observation (Fig. 1). At higher energy inputs (1500 J and 1750 J), weld specimens for both joints were subjected to higher temperatures under larger vibration amplitudes for a longer time. This led to increased diffusion between Al and Fe for Al-to-ASTM A36 steel joints and more Zn interlayer being squeezed out (Figs. 1(a), (c), and (e)) for galvanized HSLA steel joints. For both joints at higher energy inputs, failure usually occurred at the edge of the nugget zone on the softer Al side, which is referred to as "transverse through-thickness crack growth" [3,18,37,38]. After applying higher welding energy (e.g., 1750 J), due to high temperatures and the outward flow of the material under the sonotrode tool indentation, the softer Al sheet experiences some extent of bending at the nugget edge [3]. This bending phenomenon creates a small micro-level crack tip at the notch of two welded sheets, leading to a higher stress concentration since the remaining cross section could no longer sustain the shear overload. The heavily deformed Al sheet eventually allowed the cracks to grow in the transverse direction, thus experienced the through-thickness crack growth [37,39]. The mode of this crack growth occurred in the transverse direction (i.e., perpendicular to the tensile loading), indicating sound bonding between the two sheets at such energy levels since the nugget zone was completely inseparable (as indicated by the arrows in (Figs. 9(c), (d), (g), and (h)). Furthermore,

it was interesting to see that the nugget edge regions were mainly showing Al on the steel side, as also observed on the Al side of the tensile failed samples (as shown in Fig. 3). This implies that cohesive failure occured in Al base metal, which indicated a stronger interface bonding strength. Macwan and Chen [39] also reported similar observations.

3.4 Lap shear tensile fractography

Figs. 10 and 11 show typical SEM images of tensile lap shear fracture surfaces of dissimilar USWed Al-to- galvanized HSLA steel and Al-to-ASTM A36 steel joints at a welding energy of 1000 J. As seen from the overall fracture surfaces of both joints (Figs. 10(a), (b) and Figs. 11(a), (b)), two distinct regions, nugget center and nugget edge, were observed. In addition, the squeeze-out effect of materials at the nugget edge can be observed, which was caused by the localized melting due to the high temperature and clamping pressure during the USW.

For Al-to-galvanized HSLA steel joints, Fig. 10(c) shows a magnified view of the box in Fig. 10(a) on the Al side at the interface between the nugget, the nugget edge and the base metal, where EDS area and line analyses were performed. The EDS area analysis showed that the nugget edge region had a composition of 78.6% Zn and 21.4% Al, which was very close to eutectic Al-Zn composition according to the Al-Zn binary phase diagram [40]. Fig. 10(e) shows the results of the EDS line analysis across the interface, where it can be seen that the nugget region were mainly composed of Al, while nugget edge region was composed of eutectic Al-Zn and a Zn layer. This confirms the results in Fig. 1(a), (c), and (e) that the liquid eutectic Al-Zn and melted Zn were squeezed out from the nugget region and solidified outside the nugget. The melted Zn layer can also be attributed the lower melting point Zn (419.6°C) compared to Al (660.4°C). The eutectic Al-Zn and Zn at the nugget edge created brazing effect, added some

strength and reduced the stress concentration at the nugget edge [12]. Similarly, EDS area and line scan analyses were performed on the steel side (Figs. 10(d) and (f)). The area scan analysis in the dashed line box of Fig. 10(d) showed that the nugget edge region had a composition of 7.9% Fe, 2.9% Al, and 89.3% Zn, indicating that there may be eutectic Al-Zn and some remaining Zn on the steel surface. The results on the EDS line scan in Fig. 10(f) confirmed this observation. Furthermore, it was interesting to see that the nugget region mainly showed Al on the steel side as also observed on the Al side. This implies that only partial cohesive failure occurred through the eutectic structure, indicating strong interface bonding.

On the other hand, from the chemical composition analysis of Al-to-ASTM A36 steel joints, it can be observed that both matching sides have Al-Fe IMCs containing regions as shown in Figs. 11(c) and (d), which are magnified views of the boxes in Figs. 11(a) and (b), respectively. The EDS area analysis of Al-to-ASTM A36 steel joints showed that the nugget edge region had a composition of 77.1% Fe and 23.4% Al in Fig. 11(c) and 75.6% Fe and 24.4% Al in Fig. 11(d), respectively, which was very close to the Fe_3Al phase and was in good agreement with the XRD results shown in Fig. 3(b). EDS line analysis across the interfaces of the Al-to-ASTM A36 steel joints also showed a similar composition of the Al and Fe phase (Figs. 11(e) and (f))). However, Fig. 11(e) shows the results of the EDS line analysis across the interface, where it is obvious that the nugget edge region was not composed of eutectic Al-Zn and a Zn layer as in the Al-to-galvanized HSLA steel joints. As seen from Figs. 11(c) to (f), the main difference between the two joints could clearly be identified by observing the lack of higher iron-containing Fe_3Al phases in Al-to-ASTM A36 steel welded joints.

3.5 Fatigue behavior and failure mode

Fig. 12 illustrates the *S-N* curves of dissimilar USWed Al-to-galvanized HSLA steel and Al-to-ASTM A36 steel joints in comparison with the USWed Al 5754-to-galvanized HSLA steel joints in Ref. 6. Two different welding energy conditions (based on the optimized fracture energy conditions (Fig. 7)), i.e., 1500 J for Al-to-galvanized HSLA steel and 1250 J for Al-to-ASTM A36 steel were used. The maximum load P_{max} was varied from 0.5 kN to 3.0 kN with an interval of 0.5 kN. It can be seen from Fig. 12 that the fatigue limit for the optimum energy condition was 0.5 kN in both cases. Overall, the fatigue lives of both welded joints appeared to be in good agreement with or somehow longer than the Al 5754-to-galvanized HSLA steel joints [3]. At higher P_{max} loads (1.5 kN to 3 kN), the fatigue life of Al-to-galvanized HSLA steel samples was higher than that of Al-to-ASTM A36 steel joints. As mentioned before in Section 3.3, the tensile joint strength of Al-to-galvanized HSLA steel was higher than that of Al-to-ASTM A36 steel (Fig. 5), and therefore, its fatigue resistance was also higher. This might be incorporated with the difference in the interlayer structure seen in the Al-to-galvanized HSLA steel weld samples (Fig. 3). During high P_{max} load conditions, interfacial failure is a dominant factor and observed due to progressive shearing at the joint, which is a result of plastic deformation due to a high cyclic stress amplitude or higher applied load (Figs. 13(a), (b), and (c)). However, at lower P_{max} loads (1.0 kN and 0.5 kN), the Al-to-ASTM A36 steel samples showed a higher fatigue resistance. In the low P_{max} load conditions, the applied stress is low enough to be elastic leading to failure by yielding at the nugget edge [41]. The nugget edge is the region of stress concentration where the triaxial stresses reached the maximum value due to both maximum shear stress and the stress arising from bending moment [42]. As mentioned above, Al-to-galvanized HSLA steel joints showed the localized stress concentration at the nugget edge resulting in nugget edge failure shown in Figs. 13(d) and (e). The difference in fatigue life (Fig. 12) of two welded joints could

be explained from their failure modes. Figs. 13 and 14 show macroimages of failed fatigue samples at 1 kN to 3 kN for both welding joints. Two main failure modes were observed in both joints, namely: (1) an interfacial failure mode as shown in Figs. 13(a), (b), and (c) and Fig. 14(e), and (2) transverse through thickness (TTT) failure as shown in Figs. 13(d) and (e) and Figs. 14(a)-(d). Generally, interfacial failure occurred in the low cycle fatigue regime ($P_{max} \geq 2$ kN), while TTT failure occurred in the high cycle fatigue regime ($P_{max} < 2$ kN) [3]. Patel *et al.* [3] and Mirza *et al.* [38] have also reported the transition from interfacial failure to TTT with decreasing loads. A similar failure mode transition trend can be observed for Al-to-galvanized HSLA steel joints as shown in Fig. 13, whereas the failure modes of Al-to-ASTM A36 steel samples is the opposite of this trend. The failure mode of Al-to-ASTM A36 steel fatigue samples transited from TTT at high P_{max} loads to a mixture of TTT and interfacial failure at low P_{max} loads (Fig. 14). The mixture of the TTT and interfacial failure may be responsible for the longer fatigue life of Al-to-ASTM A36 steel samples at low P_{max} loads (1.0 kN and 0.5 kN).

Fig. 15 shows the logarithmic *S-N* plots in the form of the maximum tensile shear cyclic stress versus the number of reversals to failure ($2N_f$) in terms of a Basquin-type relationship for Al-to-galvanized HSLA steel joints and Al-to-ASTM A36 steel joints. It should be noted that since there were no run-out data of non-failed samples at or over 1×10^7 cycles, all of the data points were included in the curve fitting. For Al-to-galvanized HSLA steel welded samples, the interfacial failure mode was observed at higher cyclic load levels with a fatigue strength coefficient of 345 MPa, while the TTT mode was observed at lower cyclic load levels with a fatigue strength coefficient of 301 MPa (Fig. 15(a)). For Al-to-ASTM A36 steel joints, the TTT mode was observed at higher cyclic load levels with a fatigue strength coefficient of 191 MPa, and a mixture of TTT and interfacial failure modes was observed at lower cyclic load levels with

a fatigue strength coefficient of 420 MPa. The difference in the fatigue strength coefficient for both joints (Al-to-galvanized HSLA steel: 345 MPa vs Al-to-ASTM A36 steel: 191 MPa) at higher cyclic load levels is actually in agreement with their static strength results (Fig. 5, where Al-to-galvanized HSLA steel joint showed higher strength than Al-to-ASTM A36 steel joints at higher energy level). The higher value of the fatigue strength coefficient at the lower cyclic load levels for Al-to-ASTM A36 steel joints was probably related to the mixture of TTT and interfacial failure mode.

3.6 Fatigue fractography

Figs. 16 and 17 show detailed SEM studies of the fracture surfaces of failed Al-to-galvanized HSLA steel joints and Al-to-ASTM A36 steel welded joints. Similar features of fatigue fracture surfaces can be observed in both welded joints, e.g., crack initiation, propagation and fast crack regions. It can be seen from Figs. 16(a) and 17(a) that the fatigue crack initiated from the inner edge of the Al sheet (marked as region "B"), propagated perpendicular to the loading direction, and as the number of cycles increased, it penetrated through the thickness of the sheet towards the outer surface for both joints. Figs. 16(b) and 17(b) show the crack initiation sites, and Figs. 16(c) and 17(c) show magnified images of the crack initiation (the boxes marked in Figs. 16(b) and 17(b)). The fast crack area is marked as region "D" in Figs 16(a) and 17(a). A large crack propagation region can be seen between regions "B" and "D", indicating that most of the fatigue life was spent in crack propagation as also observed by others [43]. The fast crack region "D" is quite small in comparison with the propagation region, indicating that sudden fracture occurred in this region. Miller *et al.* [44] also suggest that the crack would have to grow longer before the applied stress intensity factor reaches the fracture toughness value of the

material in the case of lower loads, resulting in a fatigue life mostly spent in crack propagation. Figs. 16(d, e) and 17(d, e)) show the fatigue striation characteristics in the crack propagation zone. Like most of the fatigued samples, both of the joints exhibited surface ripples or fatigue striations in the fatigue crack propagation zone, which were nearly perpendicular to propagation direction. Generally, in face-centered cubic materials, fatigue striations normally occur via a repeated plastic blunting-sharpening process within the plastic zone ahead of the fatigue crack tip [31]. This process mainly stems from the glide of dislocations on the slip plane along the slip direction.

4. Conclusions

Dissimilar USWed Al 6061-to-galvanized HSLA steel and Al 6061-to-ASTM A36 steel joints at different levels of welding energy have been explored in terms of interface microstructure, tensile lap shear strength and fatigue properties. The following conclusions can be drawn:

1. Microstructure observations revealed that the θ ($FeAl_3$) phase was present at the weld interface for both dissimilar joints, while the Al-Zn eutectic layer was present at the interface in the Al-to-galvanized HSLA steel joints and the Fe_3Al layer was present at the interface in the Al-to-ASTM A36 steel joints.
2. The average peak welding strength and fracture energy of the Al-to-galvanized HSLA steel welded joints were higher than those of the Al-to-ASTM A36 steel welded joints. The joint strengths of both USWed Al-to-steel welds were higher than those of other Al-to-steel combinations using various welding techniques reported in the literature.

3. Most of the tensile failure at low energy inputs occurred from the Al/Fe interface, whereas the failure mode became the transverse through-thickness crack growth at high welding energy inputs, which occurred at the edge of the nugget zone on the softer Al side.
4. For both Al-to-galvanized HSLA steel and Al-to-ASTM A36 steel welded joints, the fatigue limit for optimum welding energy was found to be 0.5 kN. The fatigue lives of both welded joints are in agreement with or somewhat longer than other Al-to-steel joints reported in the literature.
5. In the case of Al-to-galvanized HSLA steel joints, the transition of the fatigue fracture mode was from transverse through-thickness crack growth to interfacial failure with increasing cyclic loads, whereas for Al-to-ASTM A36 steel joints, the weld samples exhibited the transverse through-thickness crack mode at high cyclic loads and a mixture of the transverse through-thickness crack and interfacial failure modes at low cyclic loads. Fatigue crack propagation was mainly characterized by the formation of fatigue striations on the fracture surfaces, which appeared to be perpendicular to the fatigue crack propagation direction.

Acknowledgements

The authors would like to thank the Natural Sciences and Engineering Research Council of Canada (NSERC) and Rio Tinto Aluminum, through the NSERC Industrial Research Chair in Metallurgy of Aluminum Transformation at the University of Québec at Chicoutimi (UQAC) for providing financial support. One of the authors (D.L. Chen) is grateful for the financial support by the Premier's Research Excellence Award (PREA), NSERC-Discovery Accelerator Supplement (DAS) Award, Canada Foundation for Innovation (CFI) and Ryerson Research Chair (RRC) program. The authors would also like to thank Messrs. A. Machin and Q. Li

(Ryerson University) and Messrs. D. Racine, E. Brideau, and P.-L. Privé (UQAC) for their assistance in the experiments.

References

[1] McNutt M. The beyond-two-degree inferno. Science 2015;349:7.

[2] Schaedler TA, Jacobsen AJ, Carter WB. Toward lighter, stiffer materials. Science 2013;341:1181-82.

[3] Patel VK, Bhole SD, Chen DL. Ultrasonic spot welding of aluminum to high-strength low-alloy steel: microstructure, tensile and fatigue properties. Metall Mater Trans A 2014;45:2055-66.

[4] Prangnell PB, Haddadi F, Chen YC. Ultrasonic spot welding aluminum to steel for automotive applications-microstructure and optimization. Mater Sci Tech 2011;27(3):617-24.

[5] Baig M, Khan AS, Choi S, Lee E. Effect of manufacturing processes and welding type on quasistatic and dynamic responses of aluminum alloys: experiments and modeling. J Dyn Behav Mater. 2015;1(3):299-314.

[6] Shi Y, Guo H. Fatigue performance and fatigue damage parameter estimation of spot welded joints of Al alloys 6111-T4 and 5753. Fatigue Frac Eng Mater Struct. 2013;36(10):1081-1090.

[7] Das H, Jana SS, Pal TK, De A. Numerical and experimental investigation on friction stir lap welding of aluminum to steel. Sci Technol Weld Join 2013;19(1):69-75.

[8] Prangnell PB, Bakavos D. Novel approaches to friction spot welding thin aluminium automotive sheet. Mat Sci Forum 2010;638-642:1237-42.

[9] Macwan A, Jiang XQ, Chen DL. Interfacial characterization of dissimilar joints between Al/Mg/Al-tri layered clad sheet to high-strength low-alloy steel. JOM 2015;67:1468-77.

[10] Bakavos D, Prangnell PB. Mechanisms of joint and microstructure formation in high power ultrasonic spot welding 6111 aluminum automotive sheet. Mater Sci Eng A 2010;527:6320-34.

[11] Gencsoy HT, Admas JA, Shigeo S. On some fundamental problems in ultrasonic welding of dissimilar metals. Weld J 1967;4:145s-153s.

[12] Haddadi F, Strong D, Prangnell PB. Effect of Zinc coatings on joint properties and interfacial reactions in aluminum to steel ultrasonic spot welding. JOM 2012;64(3):407-13.

[13] Watanabe T, Sakuyama H, Yanagisawa A. Ultrasonic welding between mild steel sheet and Al-Mg alloy sheet. J Mater Process Technol 2009;209:5475-80.

[14] Haddadi F. Rapid intermetallic growth under high strain rate deformation during high power ultrasonic spot welding of aluminium to steel. Mater Des 2015;66:459-72.

[15] Haddadi F, Abu-Farha F. Microstructural and mechanical performance of aluminium to steel high power ultrasonic spot welding. J Mater Proce Tech 2015;225:262-74.

[16] Springer H, Kostka A, dos Santos JF, Raabe D. Influence of intermetallic phases and Kirkendall-porosity on the mechanical properties of joints between steel and aluminum alloys. Mater Sci Eng A 2011;528:4630-42.

[17] Chen YC, Bakavos D, Gholinia A, Prangnel PB. HAZ development and accelerated post-weld natural ageing in ultrasonic spot welding aluminum 6111-T4 automotive sheet. Acta Mater 2012;60:2816-28.

[18] Xu L, Wang L, Chen Y-C, Robson JD, Prangnell PB. Effect of interfacial reaction on the mechanical performance of steel to aluminum dissimilar ultrasonic spot welds. Metall Mater Trans A 2016;47A:334-46.

[19] Zhu YH, General Rule of Phase Decomposition in Zn-Al Based Alloys (II) - On Effects of External Stresses on Phase Transformation. Mater Trans 2004:45(11): 3083-97.

[20] Ueda K, Ogura T, Nishiuchi S, Miyamoto K, Nanbu T, and Hirose A. Effects of Zn-based alloys coating on mechanical properties and interfacial microstructures of steel/aluminum alloy dissimilar metals joints using resistance spot welding. Mater Trans 2011:52-5:967-73.

[21] Rana R, Lahaye C, Ray RK. Overview of lightweight ferrous materials: strategies and promises. JOM 2014;66:1734-46.

[22] Lee CY, Choi DH, Yeon YM, Jung SB. Dissimilar friction stir spot welding of low carbon steel and Al-Mg alloy by formation of IMCs. Sci Technol Weld Join 2009;14(3):216-20.

[23] Watanabe M, Feng K, Nakamura Y, Kumai S. Growth manner of intermetallic compound layer produced at welding interface of friction stir spot welded aluminum/steel lap joint. Mater Trans 2011;52(5):953-59.

[24] Chen YC, Nakata K. Effect of the surface state of steel on the microstructure and mechanical properties of dissimilar metal lap joints of aluminum and steel by friction stir welding. Metall Mater Trans A 2008;39A:1985-92.

[25] Shi H, Qiao S, Qiu R, Zhang X, Yu H. Effect of welding time on the joining phenomena of diffusion welded joint between aluminum alloy and stainless steel. Mater Manu Proc 2012;27(12):1366-69.

[26] Qiu R, Shi H, Zhang K, et al. Interfacial characterization of joint between mild steel and aluminum alloy welded by resistance spot welding. Mater Charact 2010;61:684-8.

[27] Qiu R, Zhang X, Hongxin, Yu H, Zhang K. Interfacial characterization of joint between mild steel and aluminum alloy welded by resistance spot welding. Adv Mater Res 2011;230-232:982-6.

[28] Lee K-J, Kumai S, Arai T. Interfacial microstructure and strength of steel to aluminum alloy lap joints welded by a defocused laser beam. Mater Trans 2005;46(8):1847-56.

[29] Jahn R, Cooper R, Wilkosz D. The effect of anvil geometry and welding energy of microstructures in ultrasonic spot welds of AA6111-T4. Metall Mater Trans A 2007;38A:570-83.

[30] Patel VK, Bhole SD, Chen DL. Microstructure and mechanical properties of dissimilar welded Mg-Al joints by ultrasonic spot welding technique. Sci Technol Weld Join 2012;17(3):202-6.

[31] Patel VK, Bhole SD, Chen DL. Improving weld strength of magnesium to aluminum dissimilar joints via tin interlayer during ultrasonic spot welding. Sci Technol Weld Join 2012;17(5):342-7.

[32] Zhang W, Sun D, Han L, Li Y. Optimised design of electrode morphology for novel dissimilar resistance spot welding of aluminum alloy and galvanized high strength steel. Mater Des 2015;85:461-70.

[33] Piccini JM, Svoboda HG. Effect of pin length on friction stir spot welding (FSSW) of dissimilar Aluminum-Steel joints. Proc Mater Sci 2015;9:504-13.

[34] Fereiduni E, Movahedi M, Kokabi AH. Aluminum/steel joints made by an alternative friction stir spot welding process. J Mater Proc Tech 2015;224:1-10.

[35] Figner G, Vallant R, Weinberger T, Enzinger N, Schröttner H, Paśič H. Friction stir spot welds between aluminium and steel automotive sheets: Influence of welding parameters On mechanical properties and microstructure. Welding in the World 2009;53(1): R13-R23.

[36] Fukumoto M, Miyagawa K, Tsubaki M, Yasui T. Spot welding between aluminum alloy and steel by friction stirring. Mater Sci Forum 2010;638-642:1227-32.

[37] Mirza FA, Macwan A, Bhole SD, Chen DL, Chen X-G. Effect of welding energy on microstructure and strength of ultrasonic spot welded dissimilar joints of aluminum to steel sheets. Mater Sci Eng A 2016;668:73-85.

[38] Mirza FA, Macwan A, Bhole SD, Chen DL. Microstructure and fatigue properties of ultrasonic spot welded joints of aluminum 5754 alloy. JOM 2016;68(5):1465-75.

[39] Macwan A, Chen DL. Ultrasonic spot welding of rare-earth containing ZEK100 magnesium alloy to 5754 aluminum alloy. Mater Sci Eng A 2016;666:139-48.

[40] Murray JL, *Bull. Alloy Phase Diagrams*, 4(1), 55-73 (1983).

[41] Cambell FC. Elements of metallurgy and engineering alloys, ASM International, 2008, Ohio, USA.

[42] Ma C, Chen DL, Bhole SD, Boudreau G, Lee A, Biro E. Microstructure and fracture characteristics of spot-welded DP600 steel. Mater Sci Eng A 2008;485:334-346.

[43] Xu W, Westerbaan D, Nayak SS, Chen DL, Goodwin F, Biro E, Zhou Y. Microstructure and fatigue performance of single and multiple linear fiber laser welded DP980 dual-phase steel. Mater Sci Eng A 2012;553:51-58.

[44] Miller WS, Zhuang L, Bottema J, Wittebrood AJ, De Smet P, Haszler A, Vieregge A. Recent development in aluminium alloys for the automotive industry. Mater Sci Eng A 2000;280(1):37-49.

Table

Table 1 Nominal chemical compositions of the materials used.

Material	Chemical composition (wt.%)												
	Mn	Si	Cu	Ni	Cr	Mg	Nb	Mo	C	S	P	Fe	Al
6061-T6	0.07	0.71	0.3	–	0.14	1.14	–	–	–	–	–	0.18	Bal.
HSLA	0.62	0.23	0.04	0.013	0.04	–	0.021	0.005	0.06	0.004	0.006	Bal.	0.04
ASTM A36	0.80	0.40	0.2	–	–	–	–	–	0.25	0.050	0.040	Bal.	–

Figures

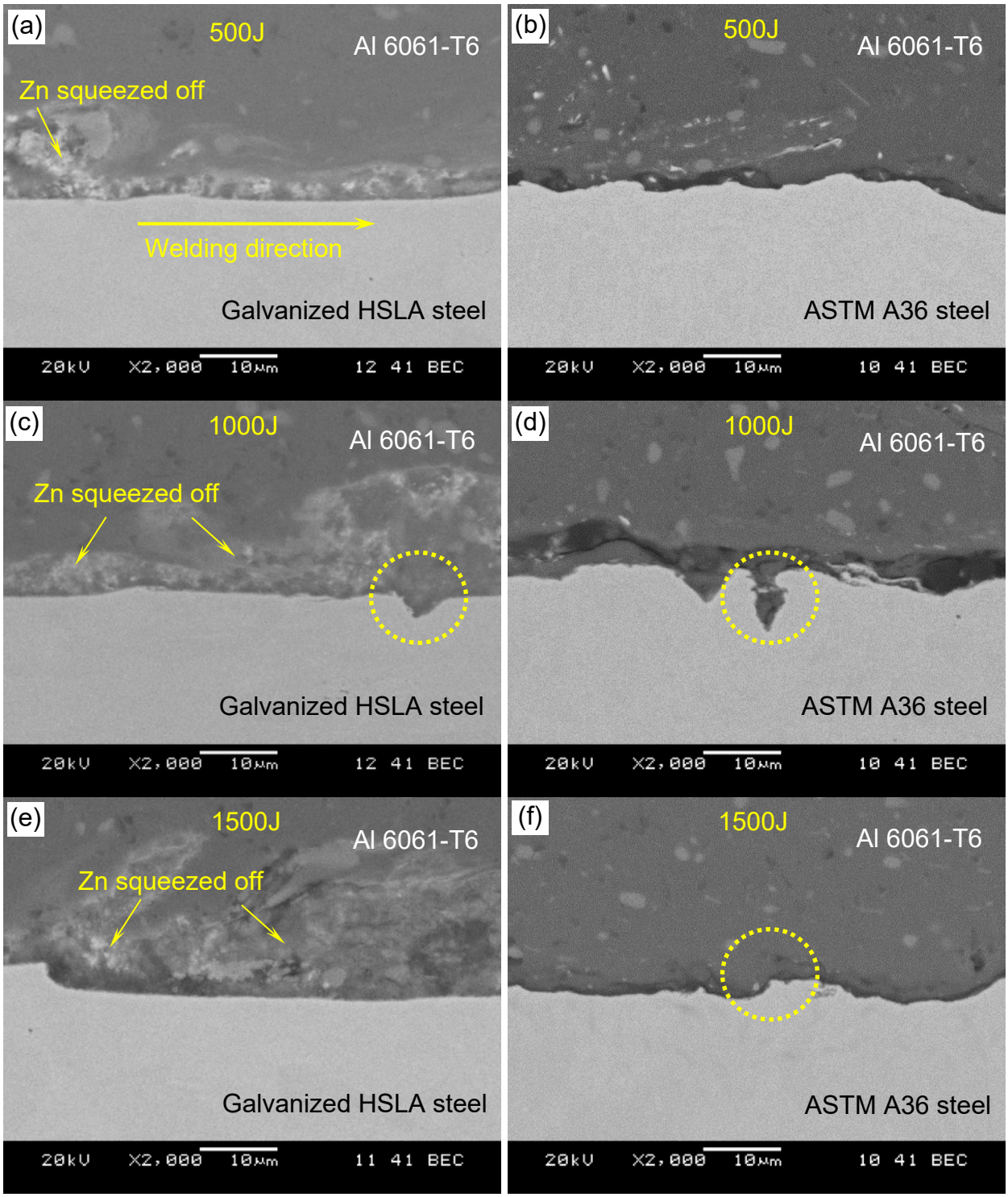

Fig. 1 SEM back-scattered electron images at the interfaces of dissimilar USWed Al 6061-to-galvanized HSLA steel joints ((a), (c), and (e)), and dissimilar USWed Al 6061-to-ASTM A36 steel joints ((b), (d), and (f)) at different energy inputs.

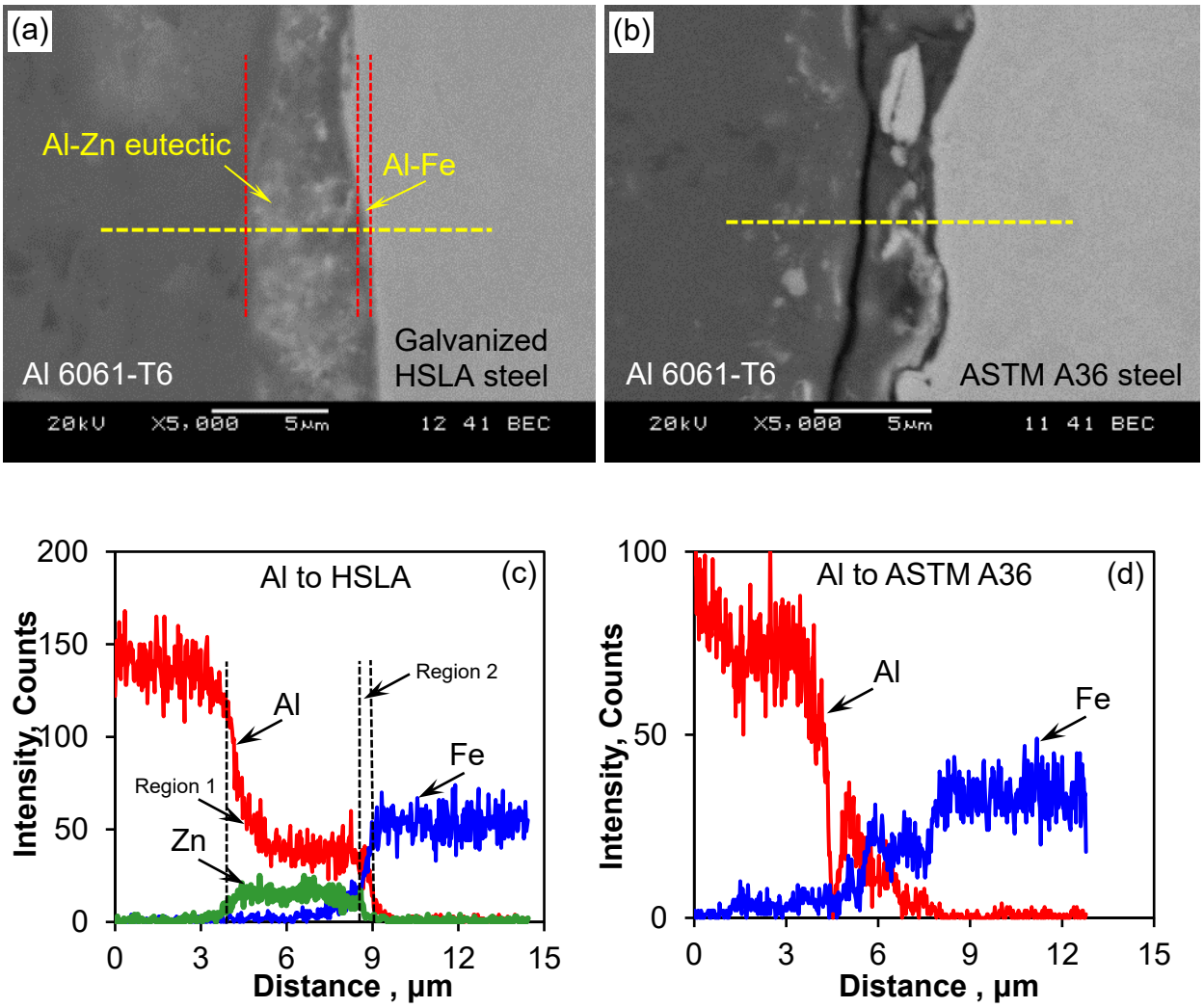

Fig. 2 SEM back-scattered electron images with EDS line scan positions and corresponding EDS results at the interfaces of dissimilar USWed Al 6061-to-galvanized HSLA steel joints ((a) and (c)) and Al 6061-to-ASTM A36 steel joints ((b) and (d)) at a welding energy of 1000 J.

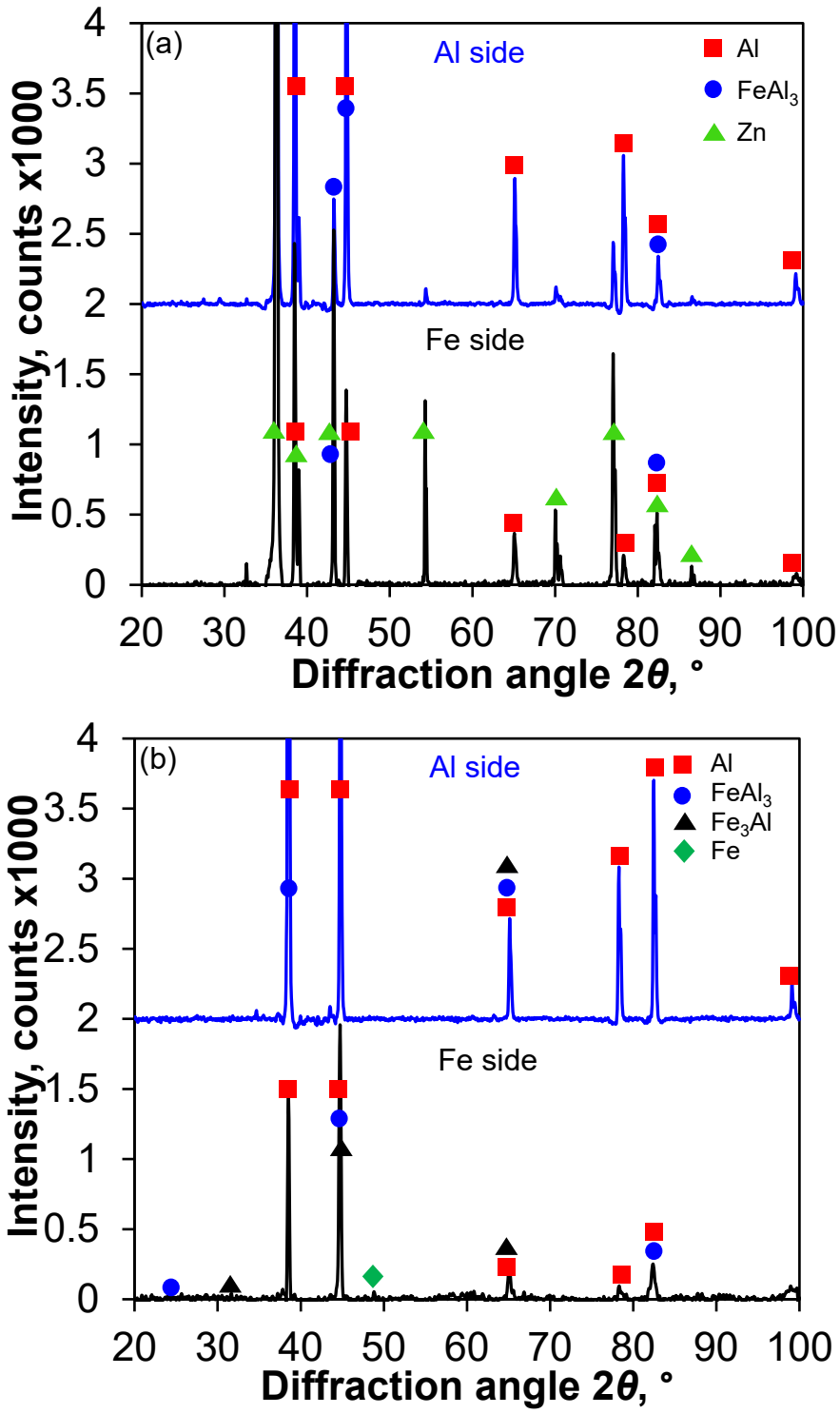

Fig. 3 XRD patterns obtained from the matching fracture surfaces of dissimilar USWed Al 6061-to-galvanized HSLA steel joints at a welding energy of 1000 J (a) and Al 6061-to-ASTM A36 steel joints at a welding energy of 1500 J (b).

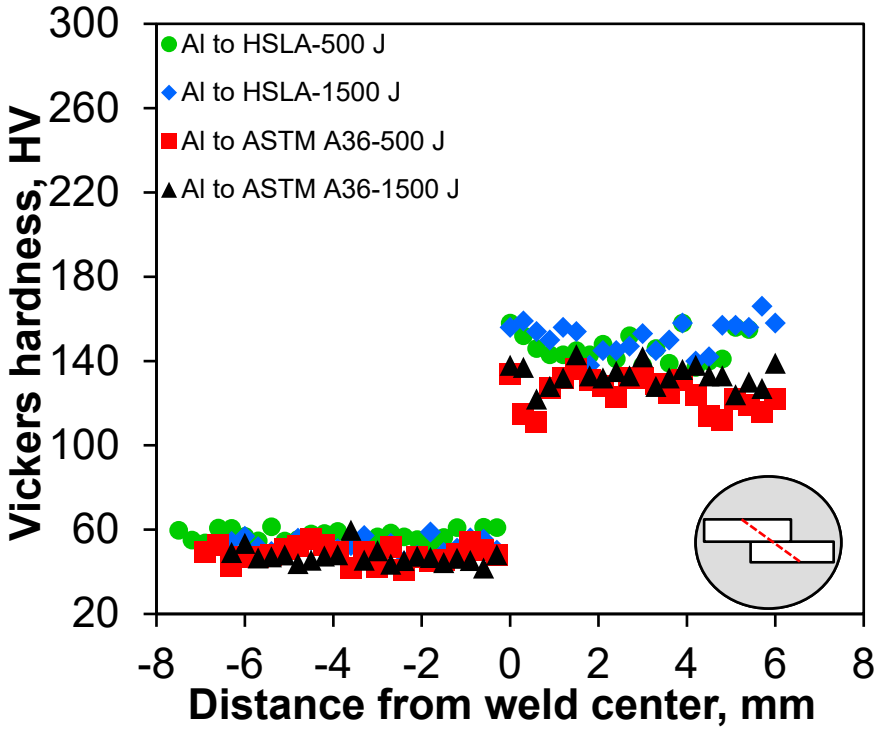

Fig. 4 Microhardness profiles across the interfaces of dissimilar USWed Al 6061-to-galvanized HSLA steel joints and Al 6061-to-ASTM A36 steel joints at different welding energy inputs.

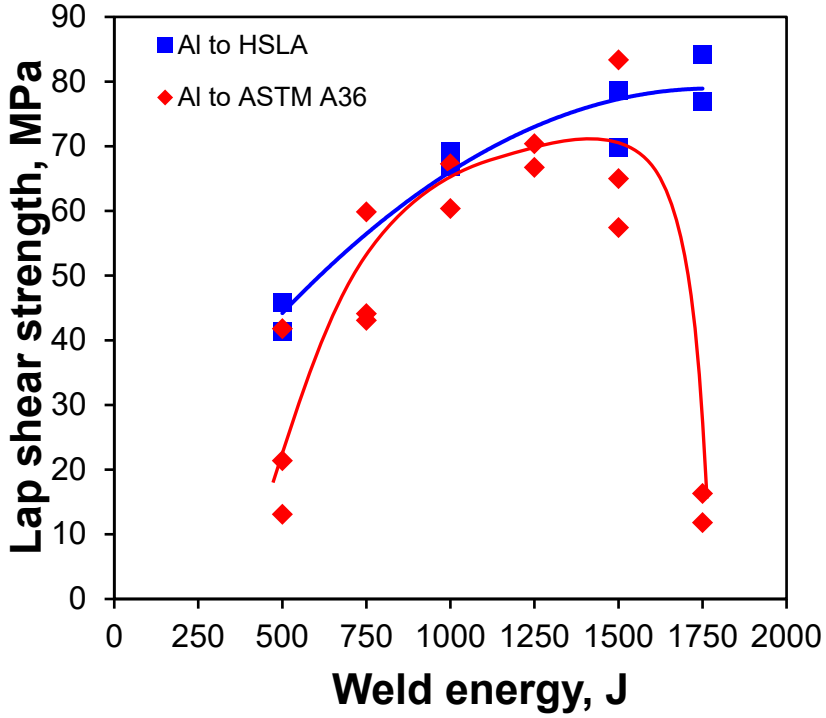

Fig. 5 Maximum tensile lap shear strengths of dissimilar USWed Al 6061-to-galvanized HSLA steel joints and Al 6061-to-ASTM A36 steel joints at different energy inputs.

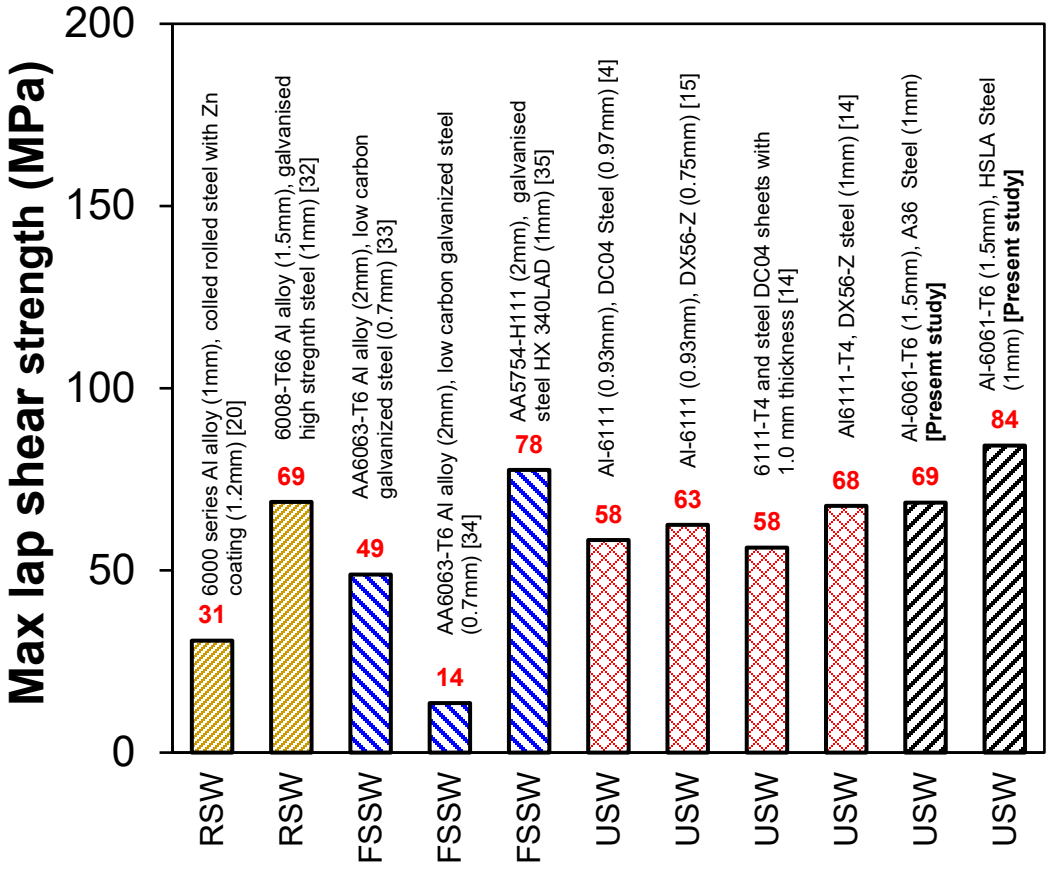

Fig. 6 Comparison of the average maximum tensile lap shear strengths of Al to steel joints using RSW, FSSW, and USW techniques [4,14,15,20,32-35].

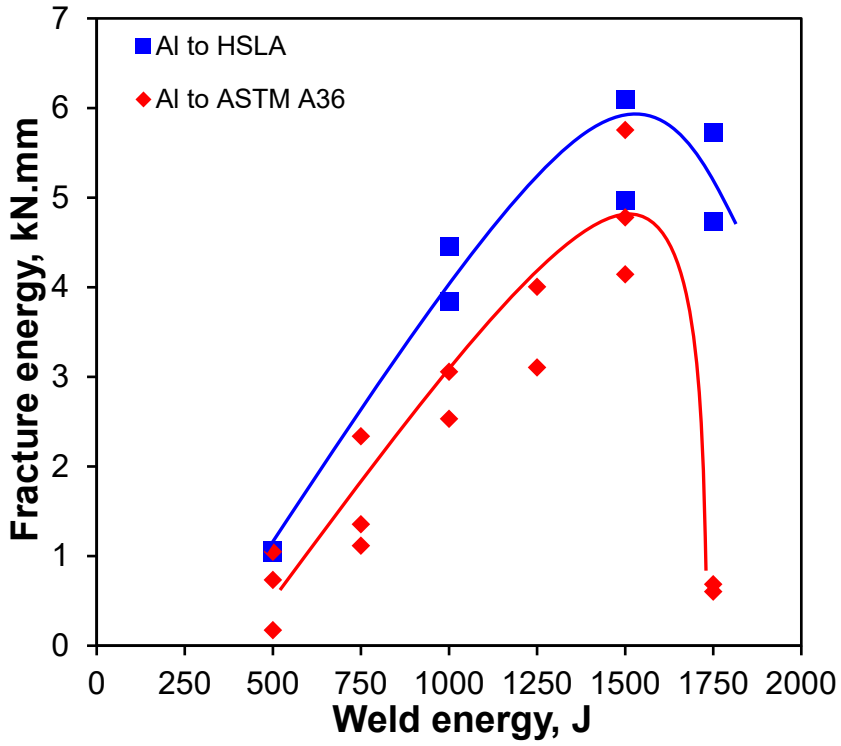

Fig. 7 Fracture energies of dissimilar USWed Al 6061-to-galvanized HSLA steel and Al 6061-to-ASTM A36 steel joints at different energy inputs.

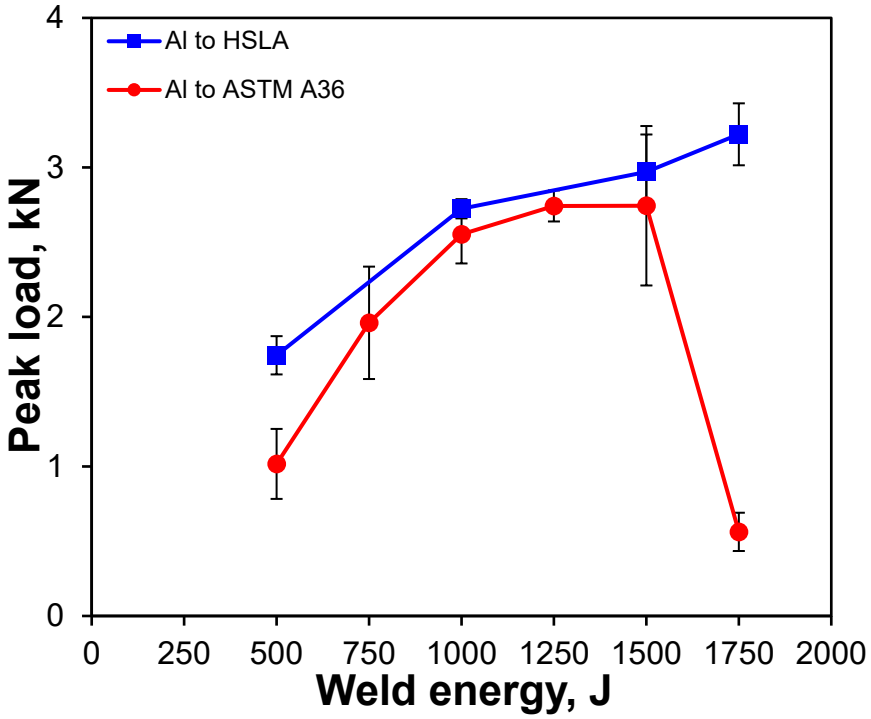

Fig. 8 Effect of welding energy on the tensile lap shear peak loads of dissimilar USWed Al 6061-to-galvanized HSLA steel and Al 6061-to-ASTM A36 steel joints.

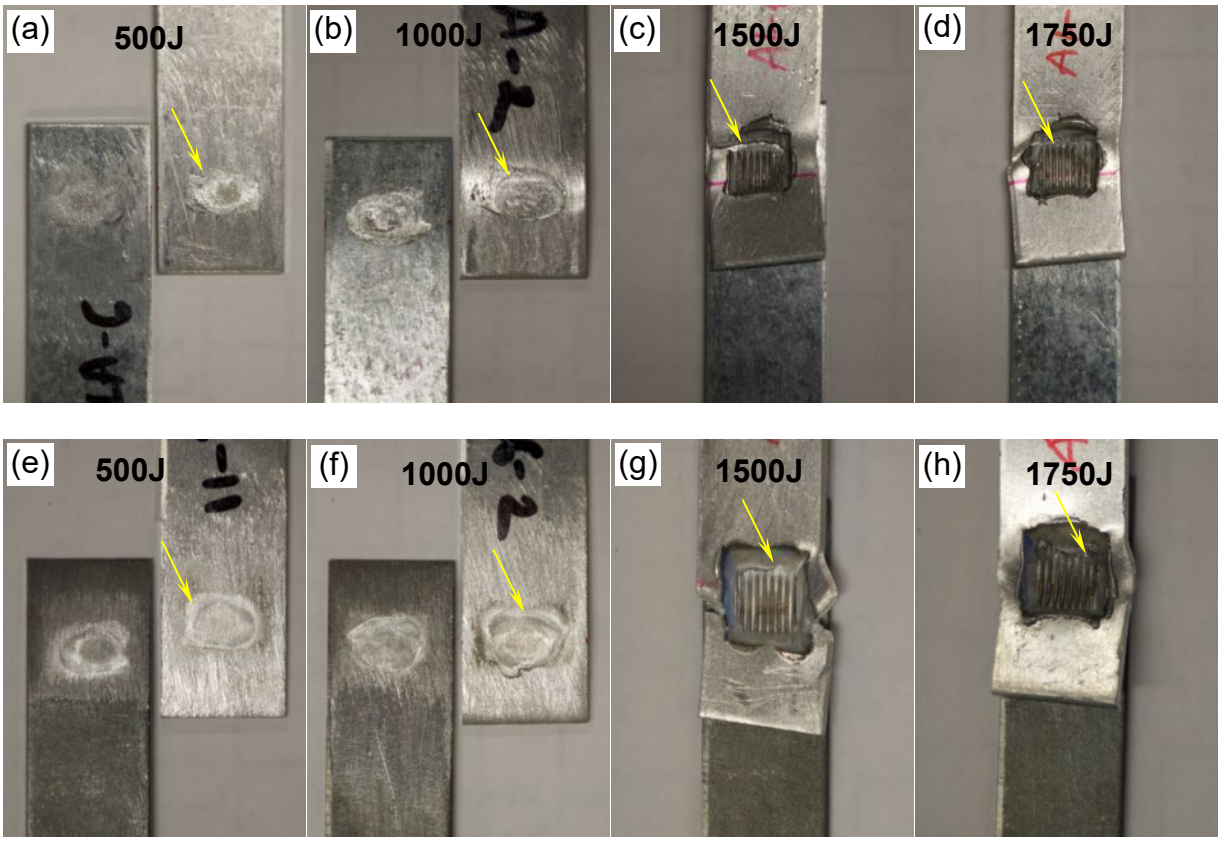

Fig. 9 Typical tensile failure locations (indicated by yellow arrows) of dissimilar USWed Al 6061-to-galvanized HSLA steel ((a)-(d)) and Al 6061-to-ASTM A36 steel ((e)-(h)) at different energy inputs.

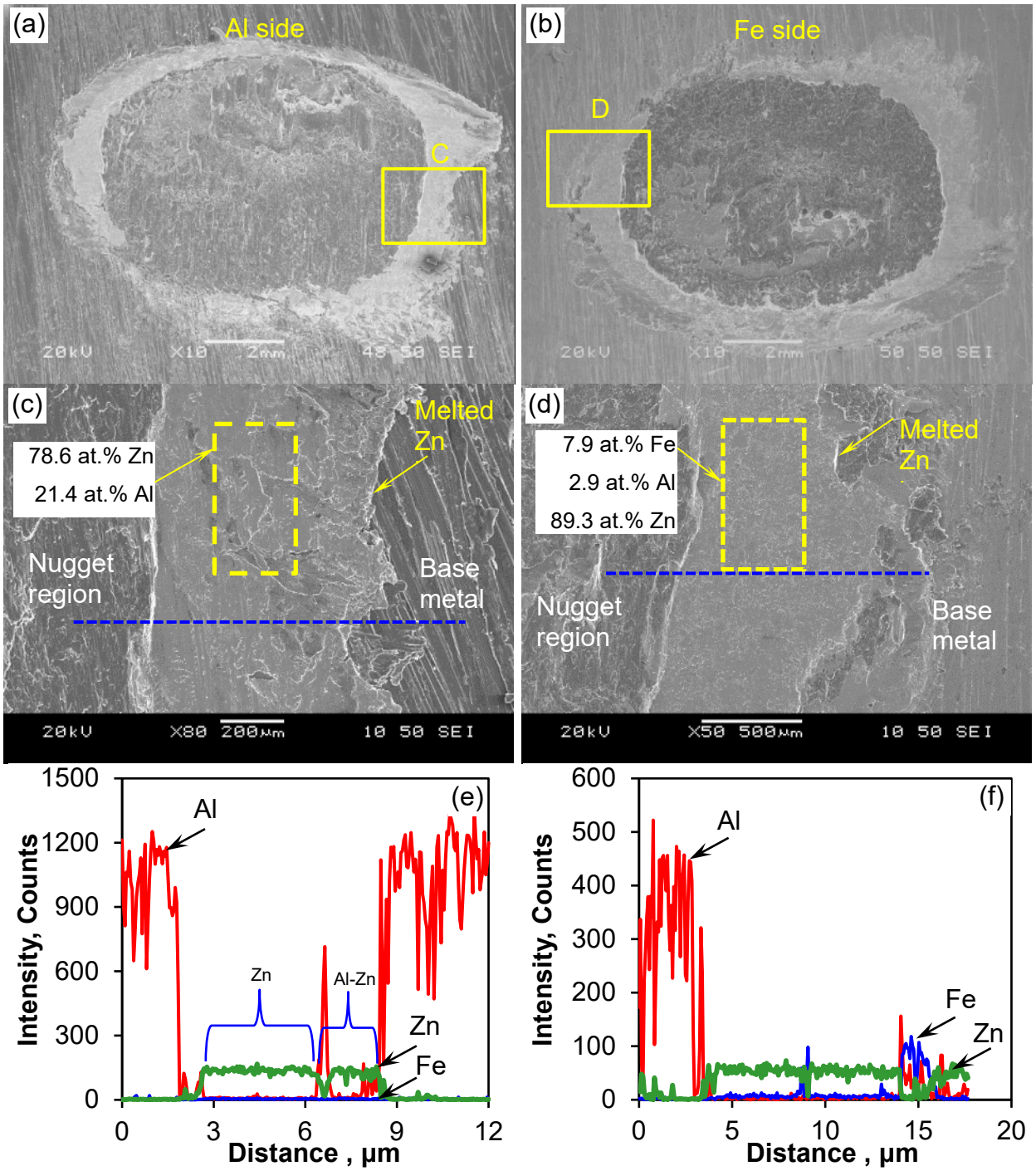

Fig. 10 Typical SEM images of tensile lap shear fracture surfaces of dissimilar USWed Al 6061-to-galvanized HSLA at 1000 J energy input: (a) overall view of Al side, (b) overall view of Fe side, (c) magnified image of the box in (a), (d) magnified image of the box in (b), (e) results of EDS line scan in (c), and (f) results of EDS line scan in (d).

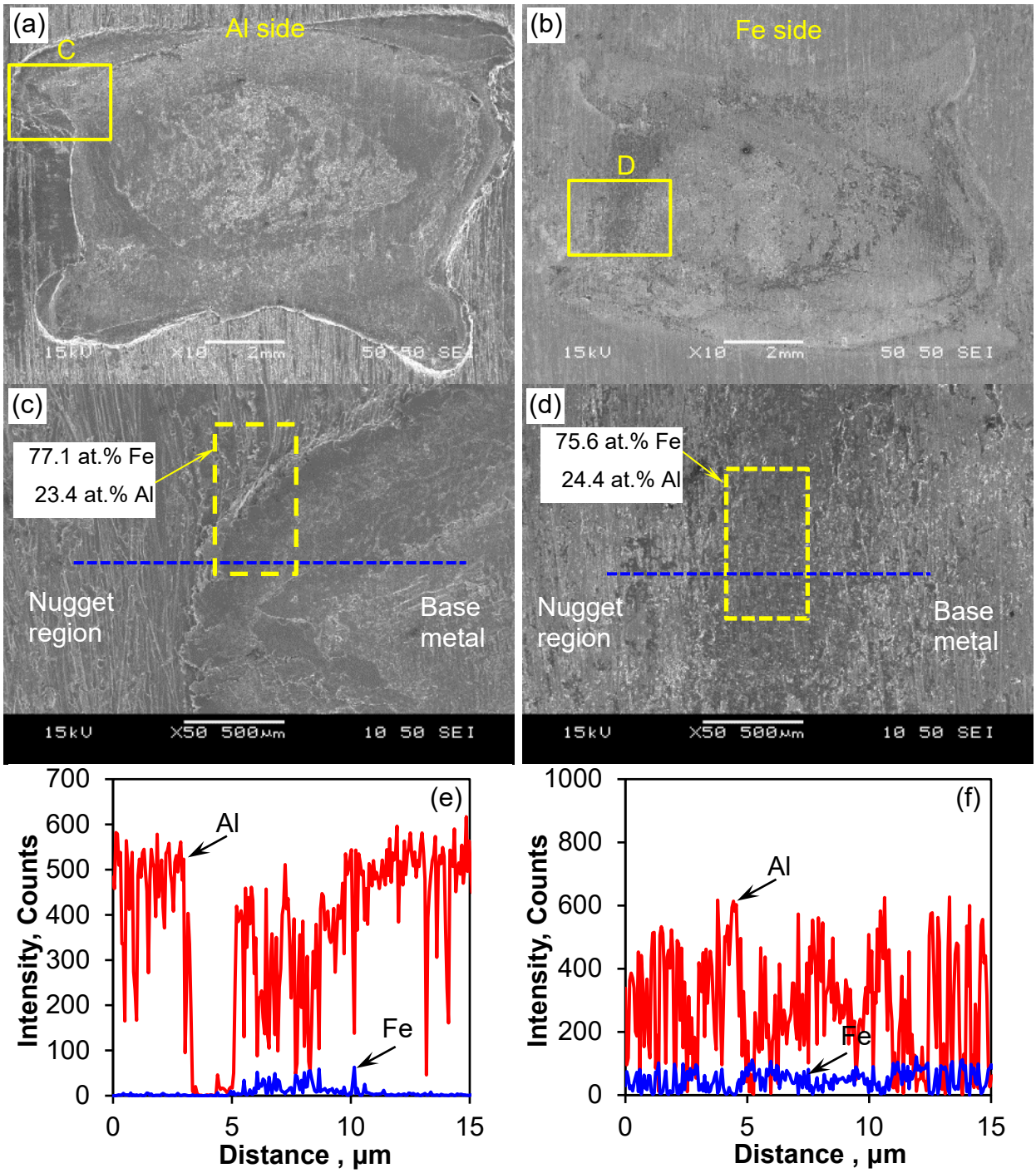

Fig. 11 Typical SEM images of tensile lap shear fracture surfaces of dissimilar USWed Al 6061-to-ASTM A36 steel at 1000 J energy input: (a) overall view of Al side, (b) overall view of Fe side, (c) magnified image of the box in (a), (d) magnified image of the box in (b), (e) results of EDS line scan in (c), and (f) results of EDS line scan in (d).

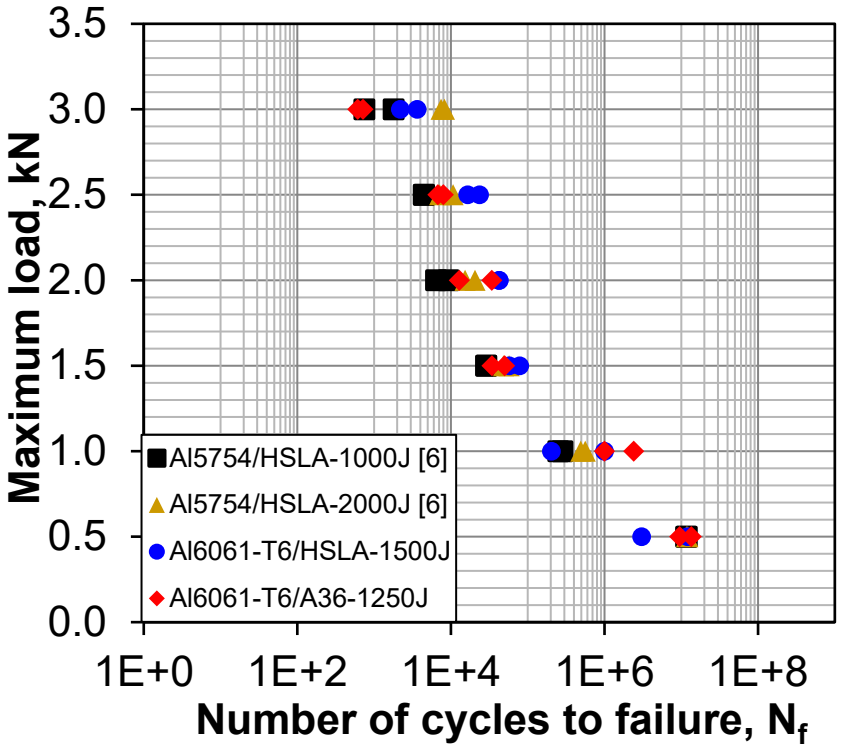

Fig. 12 *S-N* curves of dissimilar USWed Al 6061-to-galvanized HSLA steel and Al 6061-to-ASTM A36 steel joints tested at RT, $R = 0.2$ and a frequency of 50 Hz.

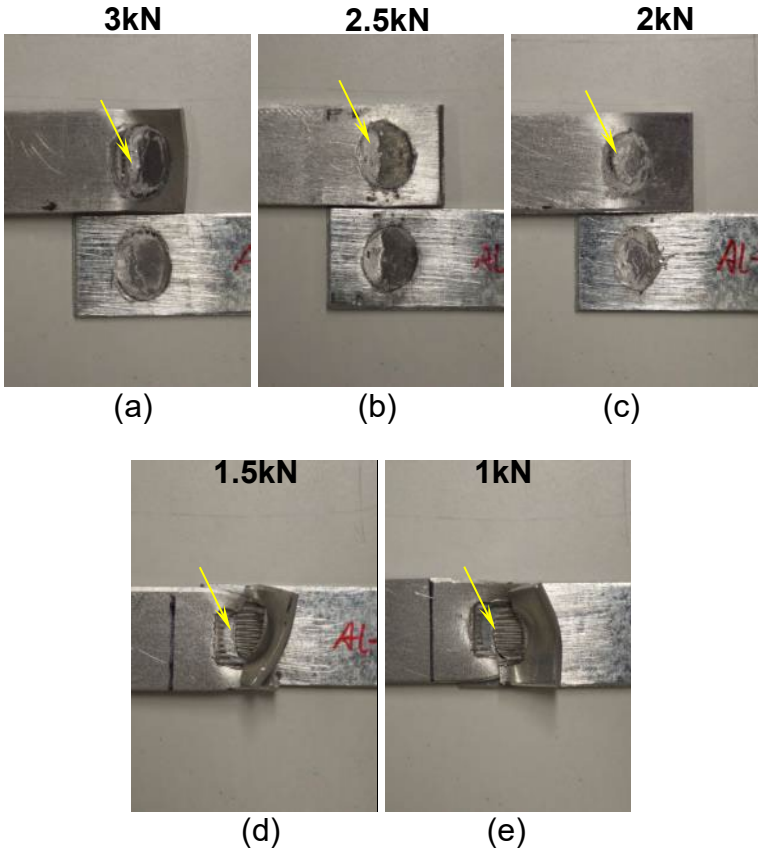

Fig. 13 Typical fatigue failure locations (indicated by yellow arrows) at different P_{max} values of dissimilar USWed Al 6061-to-galvanized HSLA steel joints at the 1500 J energy input: 3 kN (interfacial failure mode) (a), 2.5 kN (interfacial failure mode) (b), 2 kN (interfacial failure mode) (c), 1.5 kN (transverse through-thickness crack growth mode (TTT)) (d), 1 kN (TTT) (e).

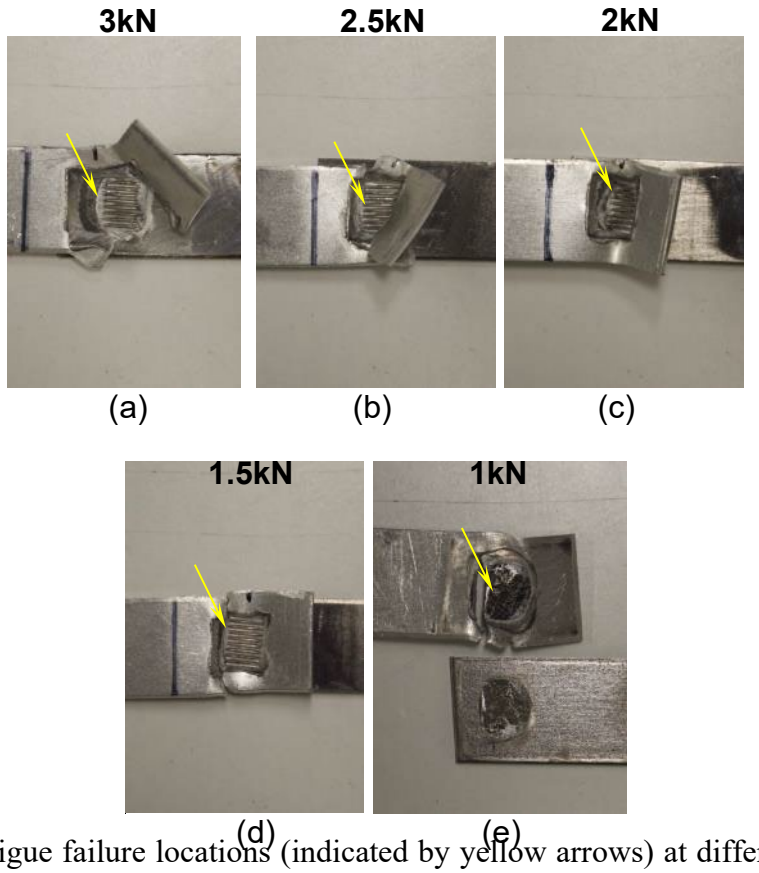

Fig. 14 Typical fatigue failure locations (indicated by yellow arrows) at different P_{max} values of dissimilar USWed Al 6061-to-ASTM A36 steel joints at the 1250 J energy input: 3 kN (transverse through-thickness crack growth mode (TTT) (a), 2.5 kN (TTT) (b), 2 kN (TTT) (c), 1.5 kN (TTT) (d), 1 kN (mixture of interfacial failure mode and TTT) (e).

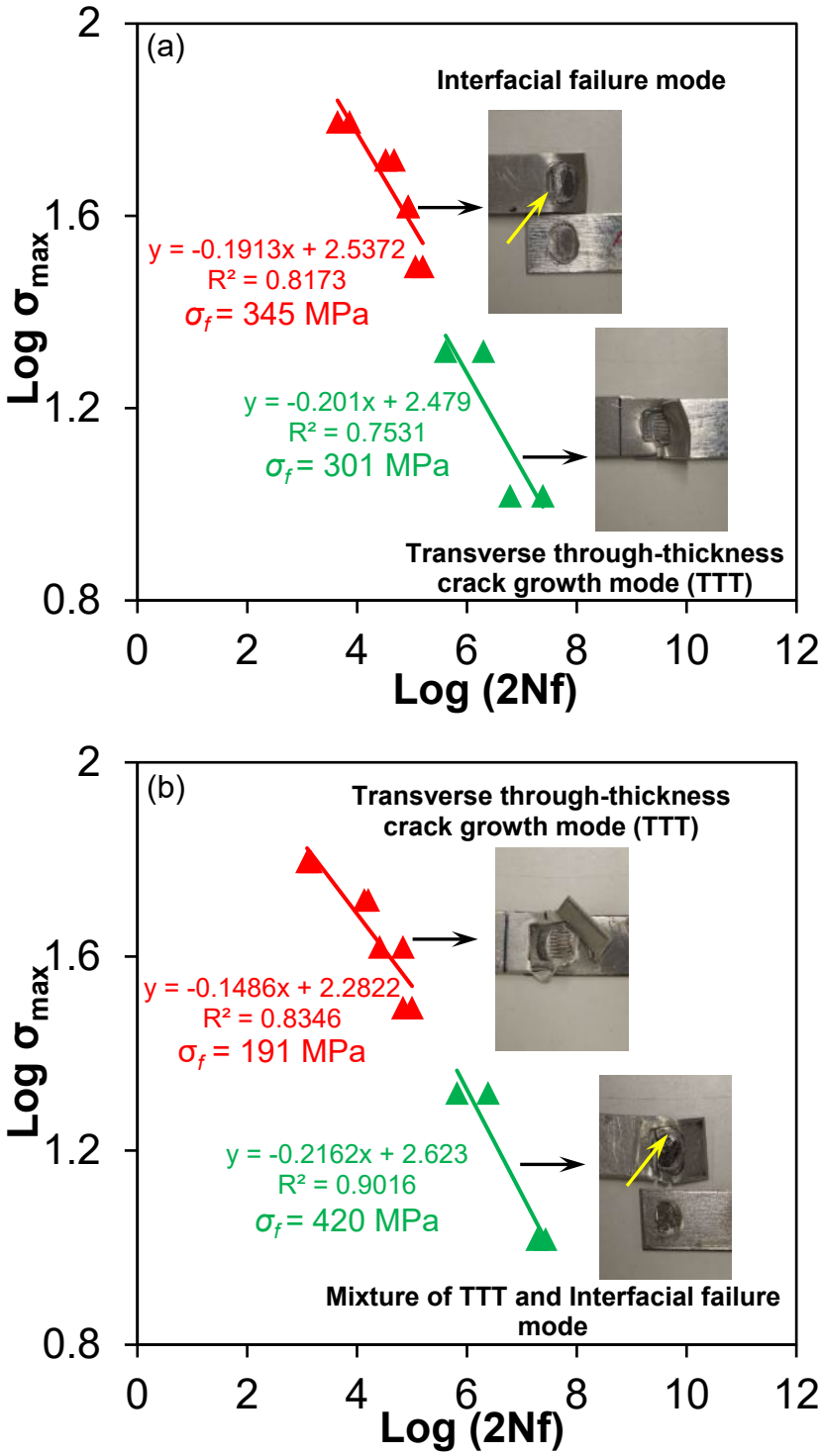

Fig. 15 The maximum tensile shear cyclic stress vs. the number of reversals to failure ($2N_f$) in the double-log scale for USWed Al 6061-T6-to-galvanized HSLA at 1500 J energy input (a) and Al 6061-T6-to-ASTM A36 steel at 1250 J energy input (b).

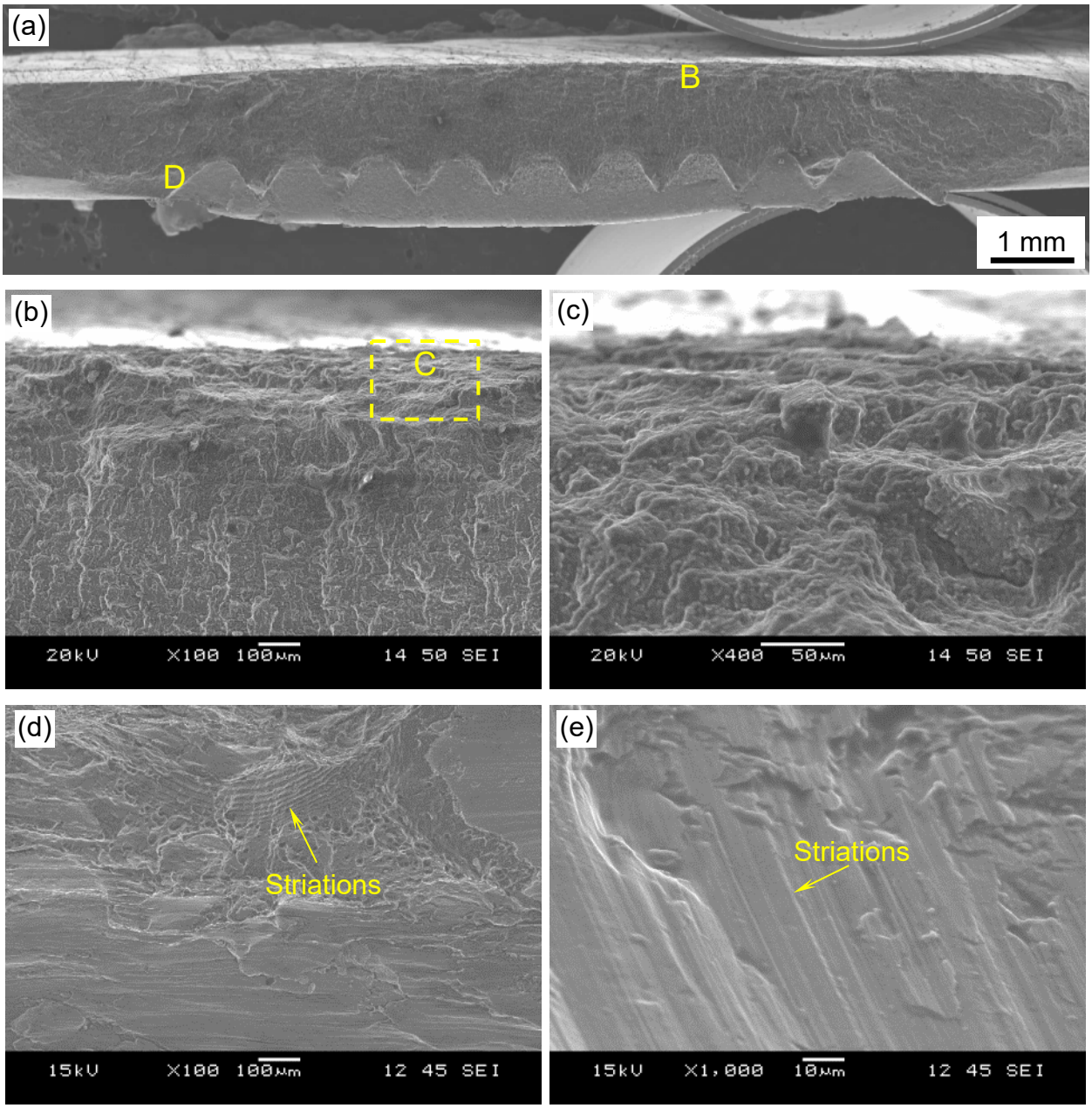

Fig. 16 Typical SEM images of fatigue fracture surface of a dissimilar USWed Al 6061-to-galvanized HSLA joint at 1500 J energy input tested at a P_{max} 2.0 kN: overall view (a), crack initiation area (b), magnified image of crack initiation area (c), fatigue striations in the crack propagation zone at lower magnification image (d) and higher magnification image (e).

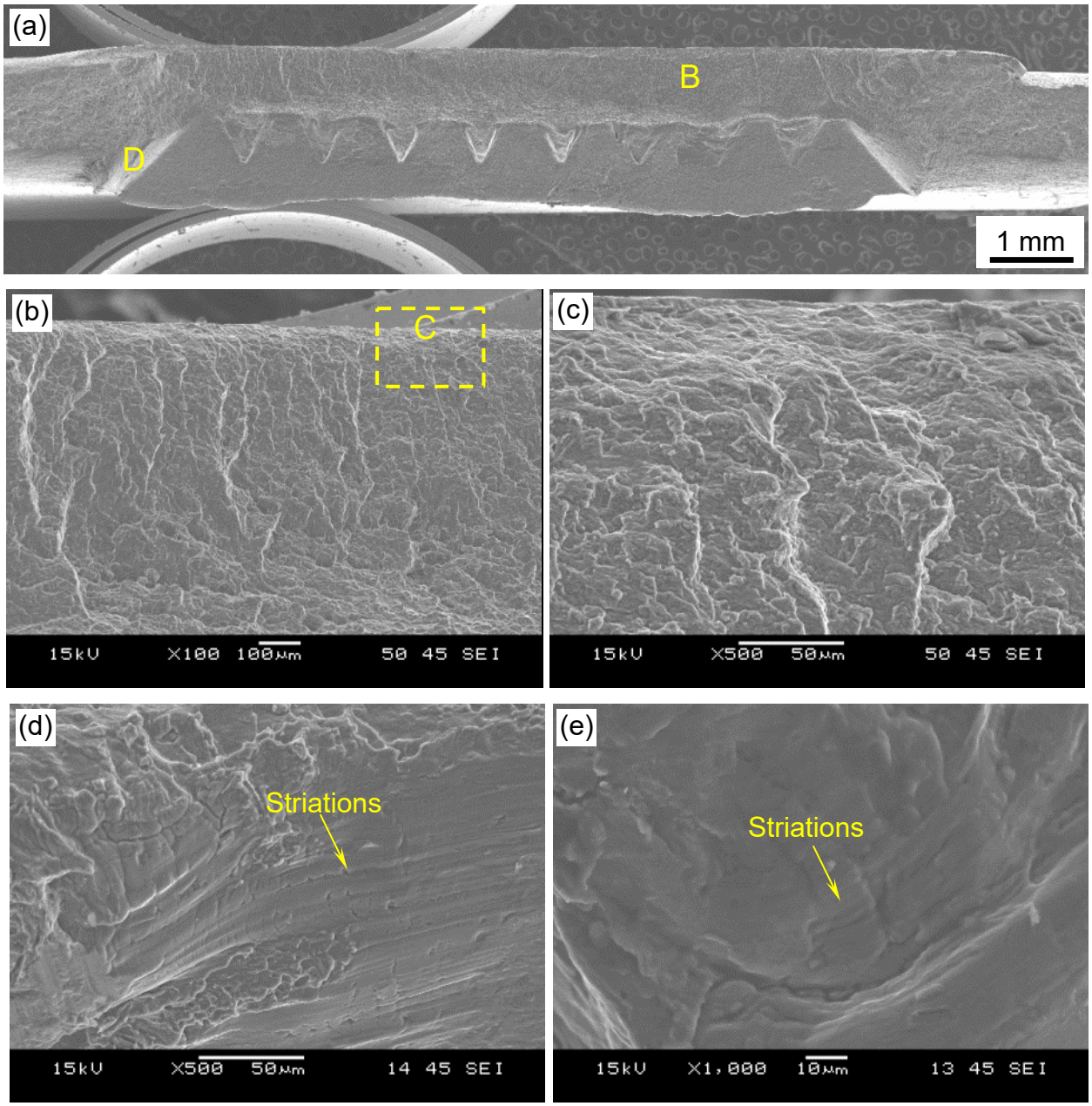

Fig. 17 Typical SEM images of fatigue fracture surface of a dissimilar USWed Al 6061-to-ASTM A36 steel joint at 1250 J energy input tested at a P_{max} 1.0 kN: overall view (a), crack initiation area (b), magnified image of crack initiation area (c), fatigue striations in the crack propagation zone at lower magnification image (d) and higher magnification image (e).